Multi-Fidelity Modeling of a Lean Premixed Swirl-Stabilized Hydrogen Burner with Axial Air Injection

Multi-Fidelity Modeling of a Lean Premixed Swirl-Stabilized Hydrogen Burner with Axial Air Injection

Lorenzo Folcarelli *, Andrea Ferrero†, Filippo Masseni ‡ and Dario Pastrone§
Politecnico di Torino, Torino, Italy, 10129

Anna Spagnolo ¶
Optimad Srl, Torino, Italy, 10134

Fausto Dicech ‖
Università degli Studi di Trieste, Trieste, Italy, 34127
Optimad Srl, Torino, Italy, 10134

Premixed hydrogen burners offer promising results in reducing pollutant emissions but are susceptible to flashback, posing significant safety risks and requiring high experimental costs. This study introduces a multi-fidelity modeling approach to address the challenges posed by the scarcity of high-fidelity data, leveraging the assumption of a linear correlation between high-fidelity and low-fidelity data. The model is tested on predicting the axial flame distance from the mixing tube, an indicator of flashback susceptibility, in a lean premixed swirl-stabilized hydrogen burner. Experimental results serve as high-fidelity data, while 2D steady axisymmetric RANS simulations provide low-fidelity data. The results demonstrate the potential of 2D RANS to approximate burner behavior accurately and the capability of the multi-fidelity model to enhance low-fidelity predictions with a severely limited set of training points.

I. Nomenclature

Roman Letters

a	=	slope of linear correlation
a_{Fl}	=	experimental constant for fuel temperature determination
b	=	intercept of linear correlation
b_{Fl}	=	experimental constant for fuel temperature determination
c_p	=	specific heat capacity at constant pressure
C_ξ	=	length scale constant
C_τ	=	time scale constant
d	=	total derivative
D	=	diameter
D_m	=	mass diffusion coefficient
D_T	=	Soret diffusion coefficient
h	=	sensible enthalpy
h^0	=	enthalpy of formation
J	=	diffusion flux
k	=	turbulent kinetic energy
$\dot{m}$	=	mass flow rate

*PhD student, Department of Mechanical and Aerospace Engineering, Corso Duca degli Abruzzi 24, Torino, Italy, AIAA Member
†Associate Professor, Department of Mechanical and Aerospace Engineering, Corso Duca degli Abruzzi 24, Torino, Italy
‡Assistant Professor, Department of Mechanical and Aerospace Engineering, Corso Duca degli Abruzzi 24, Torino, Italy, AIAA Member
§Full Professor, Department of Mechanical and Aerospace Engineering, Corso Duca degli Abruzzi 24, Torino, Italy, AIAA Associate Fellow
¶Corporate researcher, Via Agostino da Montefeltro 2, Torino, Italy
‖PhD Student, Department of Engineering and Architecture, Via Alfonso Valerio 6/A, Trieste, Italy

$\mathcal{M}$ = molecular weight
p = pressure
Pr_t = turbulent Prandtl number
r = radial distance
R = universal gas constant
$\mathcal{R}$ = volumetric rate of creation
S = strain rate tensor
Sc_t = turbulent Schmidt number
T = temperature
u_0 = mean air axial velocity in the mixing tube without fuel injection
v = velocity
$\dot{V}$ = volume flow rate
x_F = axial flame distance from the mixing tube
y_{LF} = low-fidelity data
y_{HF} = high-fidelity data
y^+ = dimensionless wall distance
Y = mass fraction
w = weight function
z = axial coordinate

Greek Letters

∂ = partial derivative
δ = function of the differences between high-fidelity and low-fidelity data
δ_{ij} = Kronecker delta with respect to indices i and j
ϵ = rate of dissipation of turbulent kinetic energy
θ = azimuth
κ = laminar thermal conductivity
κ_{eff} = effective thermal conductivity
κ_{fs} = volume fraction
μ = laminar dynamic viscosity
μ_t = turbulent dynamic viscosity
μ_{eff} = effective dynamic viscosity
ν = kinematic viscosity
ξ = length scale
ρ = density
τ = turbulent stress tensor
τ^* = time scale
ϕ = equivalence ratio
χ = axial injection ratio
Ω = volumetric heat of reaction

Abbreviations

AHEAD = Advanced Hybrid Engines for Aircraft Development
EDC = Eddy Dissipation Concept
HF = High-Fidelity
LES = Large Eddy Simulation
LF = Low-Fidelity
RANS = Reynolds Averaged Navier Stokes
RBF = Radial Basis Function
RMSE = Root Mean Square Error

II. Introduction

As the aeronautical world is moving toward a more environmentally conscious future, hydrogen-fueled propulsion emerges as both a compelling alternative to hydrocarbon fuels and a multifaceted challenge. The attraction lies in the possibility of achieving efficient combustion within gas turbine engines, thanks to hydrogen's high lower heating value (LHV) and specific heat [1]. Moreover, the carbon-free products resulting from hydrogen combustion promise a cleaner aviation landscape. However, this promising path is not without obstacles. In addition to the extreme difficulties of storing hydrogen on board and the additional weight caused by hydrogen tanks, elevated temperatures in the combustion chamber can cause the emission of nitrogen oxides (NO_x) [2], which endanger both environmental and human health. To mitigate the formation of NO_x emissions, a possible solution lies in operating under conditions of a premixed low equivalence ratio, i.e. a lean combustion regime, as the wide range of flammability of hydrogen, much wider than that of Jet-A fuel, allows for this kind of flexibility [3]. However, it is essential to recognize that operating in lean conditions can provoke combustion instabilities [4]. Additionally, hydrogen's high laminar flame speed and diffusivity lead to a propensity for upstream flame propagation in hydrogen-premixed systems, i.e. flashback [5]. As flashback can lead to altered combustion processes, pollutant emissions, and potential damage to the walls, its assessment is of the utmost importance when evaluating the performance of an hydrogen burner [6].

In the present work, a multi-fidelity model is presented and used to predict the axial flame position in different working conditions for the AHEAD lean premixed swirl-stabilized hydrogen burner [7]. The flame distance from the mixing nozzle is considered a marker of the safety margin of flashback since in this kind of burner the axial position of the flame front shifts upstream as it approaches the conditions where flashback occurs [8]. It is, therefore, chosen as the objective of the multi-fidelity model. The work is organized in the following way: in Sec.III the multi-fidelity model is presented, while Sec.IV shows the features of the burner selected as the test case. Then, Sec.V shows the procedure to obtain low-fidelity data through RANS and an assessment of CFD capability to approximate experimental results. Finally, the results of the multi-fidelity model are presented in Sec.VI.

III. Multi-Fidelity Model

The multi-fidelity modeling [9] is carried out using experimental data from Ref.[8] as high-fidelity data and 2-D axisymmetric swirl RANS simulation as low-fidelity data. Multi-fidelity consists of a series of machine learning techniques widely used to solve regression and interpolation problems. Usually, these models are based upon Gaussian Processes (GP) [10] or artificial neural networks [11]. The general objective of multi-fidelity is to improve the accuracy of an approximation model, reducing the overall computational cost associated to the training data. This can be achieved by leveraging the contribution of information coming from heterogeneous sources. Typically, few high-fidelity data are paired with many low-fidelity data, assuming a correlation between low- and high-fidelity information. This allows to better approximate unknown high-fidelity configurations, if compared to an equivalent single fidelity model, lowering the overall cost. In general, low-fidelity data are cheaper than high-fidelity data, however low-fidelity is, by definition, less accurate.

Let x_{HF} and y_{HF} be the high-fidelity (HF) input-output data for the regression problem. Similarly, x_{LF} and y_{LF} are the low-fidelity (LF) input-output data. The proposed method assumes that the training sets $X_{HF} = \{x^i_{HF} : i = 1, \dots, n\}$ and $X_{LF} = \{x^i_{LF} : i = 1, \dots, m\}$ are nested, so that $X_{HF} \subset X_{LF}$. Furthermore, if the corresponding low- and high-fidelity outputs are linearly correlated, it is possible to evaluate such relationship, as in Equation 1.

$$y_{HF} \sim a \cdot y_{LF} + b \tag{1}$$

where $a, b \in \mathbb{R}$.

Through least squares it is possible to retrieve the best approximating values for the correlation coefficients a, b. Knowing the HF and LF values for the HF training inputs $x^i_{HF} \in X_{HF}$, namely y^i_{HF} and y^i_{LF} for $i = 1, ..., n$, with n the number of HF points, we can solve for a, b the system of equations in 2.

$$\begin{bmatrix} y^1_{LF} & 1 \\ \dots & \dots \\ y^n_{LF} & 1 \end{bmatrix} \begin{bmatrix} a \\ b \end{bmatrix} = \begin{bmatrix} y^1_{HF} \\ \dots \\ y^n_{HF} \end{bmatrix} \tag{2}$$

Found a, b and considering any LF value $y_{LF}(x)$, with x being a point in the input domain, it is possible to obtain a first approximation $y^*_{HF}(x)$, as in Equation 3

$$y_{HF}(x) \sim y^*_{HF}(x) = a \cdot y_{LF}(x) + b \tag{3}$$

where $y_{LF}(x)$ can be accurately approximated with a surrogate model (given the lower computational cost) or computed online if the model is cheap enough.

In general, $y^*_{HF}(x)$ will not fit perfectly the HF training points, therefore this approximation should be corrected. To this end, the objective is to create a model trained on the differences δ between $y^*_{HF}(x)$ and the known values $Y_{HF} = \{y^i_{HF} : i = 1, \dots, n\}$. The function $\delta(x)$ is known only in the training points

$$\delta^i = y^i_{HF} - y^*_{HF}(x^i_{HF}) \qquad \forall\, i = 1, ..., n \tag{4}$$

and can be approximated with an interpolator, such as a Radial Basis Functions (RBF) or a Gaussian Process (GP) regression [12, 13]. This allows to approximate $y_{HF}(x)$ as in Equation 5

$$y_{HF}(x) \sim y^*_{HF}(x) + \delta(x) \tag{5}$$

Note, however, that multi-fidelity models are often used when there is lack of HF information, therefore the model $\delta(x)$ is not expected to be accurate far away from the training points. In fact, a possible solution is to use a weight function $w(x)$ to scale the contribution of the δ term, as in Equation 6:

$$y_{HF}(x) \sim y^*_{HF}(x) + \delta(x) \cdot w(x) \qquad . \tag{6}$$

The weight function should represent a measure of "closeness" between a generic point x and the training points. The intuition is that points which are closer to each other in the input domain should have a stronger effect, compared to those farther away. In this model, the simplest yet effective choice was to set the weights to decrease as the distance between x and the training points increases.

This multi-fidelity model has been implemented in the software romBOX developed by Optimad Srl [14].

IV. Test Case Description

The multi-fidelity model is designed to predict the flame distance from the exit of the mixing tube, utilizing the experimental measurements conducted in the 'Advanced Hybrid Engines for Aircraft Development' (AHEAD) combustor, developed by Paschereit et al. [8], as high-fidelity data. The AHEAD combustor features a fuel conduit that injects hydrogen into the premixing section through 16 axial injection orifices, each with a diameter of 0.8 mm. Air is supplied to the premixing section via an air plenum, which incorporates a radial swirl generator and a variable-diameter axial orifice. The ratio between the air volume flow rate $\dot{V}$ passing through the axial orifice and the total inlet volume flow rate is defined as the axial injection ratio χ:

$$\chi = \frac{\dot{V}_{axial}}{\dot{V}_{axial} + \dot{V}_{swirl}} \tag{7}$$

The magnitude of the χ parameter is influenced by the pressure loss in the mixing nozzle, which depends on the variable diameter of the axial orifice and the operating conditions [15]. The mixing tube itself is a cylindrical duct with a diameter of 34 mm, leading into a larger cylindrical chamber with a diameter of 105 mm. Additionally, a small fraction of the air entering the air plenum is injected at the end of the mixing tube through 22 orifices, each with a diameter of 0.6 mm, to locally reduce the equivalence ratio near the wall and prevent wall flashback. A CAD representation of the AHEAD combustor is provided in Fig. 1, while a detailed description of its features is available in Ref. [16].

The operating conditions of the combustor are determined by the air inlet mass flow, air temperature, equivalence ratio, geometrical swirl number and axial inlet diameter. The geometrical swirl number, which excludes the contribution of incoming axial air in its definition, is adjusted by modifying the portion of the radial swirl generator occupied by blocking rings: all the data referred in this work are performed at a swirl number of 0.9. Hydrogen, stored at room temperature, enters the combustor at a temperature that can be approximated based on the air mass flow, equivalence ratio, and air temperature, as described in Ref. [8]. This relationship is given by:

$$T_{H_2} = \frac{a_{Fl}\, T_{in} + b_{Fl} \left(\dot{m}_{H_2}\, c_{p,H_2} - 0.5\, a_{Fl} \right)}{0.5\, a_{Fl} + \dot{m}_{H_2}\, c_{p,H_2}} \tag{8}$$

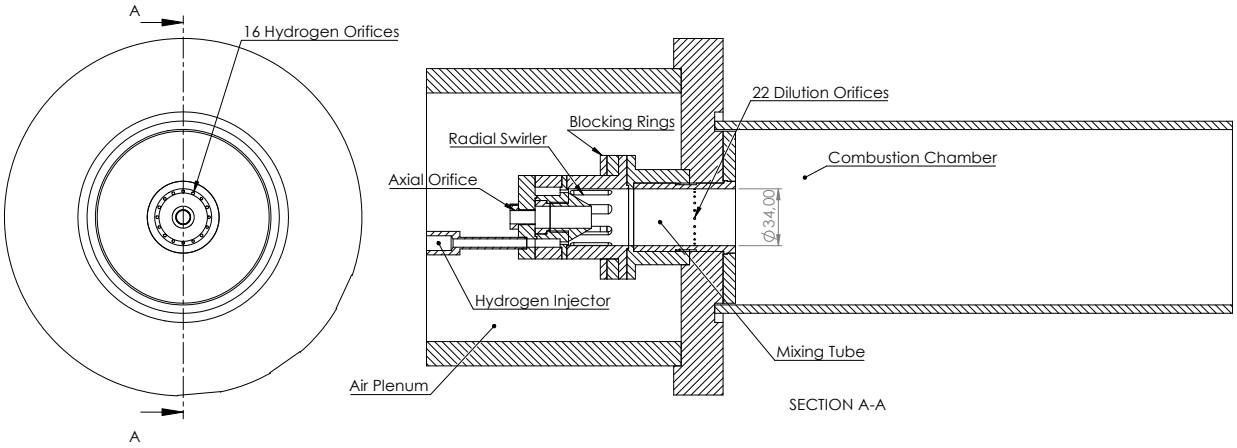

Fig. 1 CAD drawing of the AHEAD combustor in a configuration with geometric swirl number equal to 0.9 and axial orifice diameter equal to 8 mm.

Here, T_{in} represents the air temperature, $\dot{m}_{\text{H}_2}$ denotes the hydrogen mass flow rate, and c_{p,H_2} is the specific heat capacity of hydrogen at constant pressure, assumed to remain constant over the temperature range of interest. The constants $a_{\text{Fl}} = 1.40$ and $b_{\text{Fl}} = 34.9$ are determined experimentally [8].

The operating parameters for this study cover the following ranges: inlet air temperature from 313 K to 693 K, inlet air mass flow rate from 80 kg/h to 255 kg/h, and equivalence ratios from 0.2 to 1. However, due to challenges in simulating a condition with an equivalence ratio of 0.2 using RANS, operating conditions with this equivalence ratio are excluded from the current analysis.

The operating conditions considered here are derived from the flame distance data presented in Figures 9 and 10 in Ref. [8]. In particular, Figure 9 in Ref. [8] illustrates the flame distance at a constant $u_0 = 70$ m/s for different inlet air temperatures and equivalence ratios, while Figure 10 in Ref. [8] depicts the flame distance at a constant equivalence ratio, with changes in inlet air temperature and mass flow rate. The parameter u_0 represents the mean velocity in the mixing tube when only air is present (i.e., equivalence ratio = 0) and is calculated as:

$$u_0 = \frac{\dot{m}_{\text{air}}}{A_{\text{mixing tube}}\,\rho_{\text{air}}} \tag{9}$$

The simulated operating conditions and corresponding experimental flame distances are summarized in Table 1. Here, x_F/D represents the flame distance from the exit of the mixing nozzle, normalized by the mixing nozzle diameter $D = 34$ mm. All simulations assume an axial injection ratio $\chi = 12.5$, which, as described in Ref. [15], corresponds to an axial inlet diameter of 8 mm. These data comprise the 53 high-fidelity operating conditions used in this study. Low-fidelity simulations under the same operating conditions are also computed to construct and validate the multi-fidelity model presented in Sec. III.

V. Low-Fidelity Data Generation

A. Numerical Model

The simulations are performed in Ansys® Fluent, using a 2D steady swirl axisymmetric flow approximation, i.e. neglecting every derivative along the azimuthal θ direction while accounting for a tangential component of velocity v_θ variable along the axial z and radial r directions.

$$\frac{\partial\,(\cdot)}{\partial\theta} = 0 \tag{10}$$

$$\vec{v}\,(z,r) = [v_z, v_r, v_\theta] \tag{11}$$

Table 1 Working conditions and corresponding flame distances normalized with mixing tube diameter, extracted from Ref.[8].

ID	$\dot{m}_{Air}$ (kg/h)	T_{Air} (K)	ϕ	x_F / D	ID	$\dot{m}_{Air}$ (kg/h)	T_{Air} (K)	ϕ	x_F / D
1	255	313	0.3	0.277	28	80	453	0.4	0.171
2	255	313	0.4	0.285	29	130	453	0.4	0.293
3	255	313	0.5	0.351	30	150	453	0.4	0.299
4	255	313	0.6	0.450	31	205	453	0.4	0.353
5	255	313	0.7	0.627	32	230	453	0.4	0.417
6	180	453	0.3	0.247	33	93	623	0.4	0.302
7	180	453	0.4	0.262	34	110	623	0.4	0.299
8	180	453	0.5	0.275	35	148	623	0.4	0.350
9	180	453	0.6	0.361	36	82	693	0.4	0.306
10	180	453	0.8	0.615	37	100	693	0.4	0.317
11	180	453	1.0	0.991	38	133	693	0.4	0.324
12	130	623	0.3	0.229	39	130	313	0.6	0.389
13	130	623	0.4	0.233	40	184	313	0.6	0.479
14	130	623	0.5	0.216	41	220	313	0.6	0.529
15	130	623	0.6	0.250	42	295	313	0.6	0.558
16	130	623	0.8	0.474	43	80	453	0.6	0.293
17	130	623	1.0	0.866	44	130	453	0.6	0.399
18	116	693	0.3	0.241	45	150	453	0.6	0.389
19	116	693	0.4	0.228	46	205	453	0.6	0.442
20	116	693	0.5	0.220	47	230	453	0.6	0.555
21	116	693	0.6	0.251	48	93	623	0.6	0.349
22	116	693	0.8	0.463	49	110	623	0.6	0.342
23	116	693	1.0	0.807	50	148	623	0.6	0.362
24	130	313	0.4	0.257	51	82	693	0.6	0.339
25	184	313	0.4	0.313	52	100	693	0.6	0.346
26	220	313	0.4	0.342	53	133	693	0.6	0.346
27	295	313	0.4	0.375					

Introducing the Favre-filtered variables, denoted by a tilde, obtained for a generic scalar ϕ as:

$$\tilde{\phi} = \frac{\overline{\rho\phi}}{\bar{\rho}} \tag{12}$$

where the overbar indicates the typical Reynolds averaging and ρ represents the density, the corresponding Navier-Stokes equations are written in compressible form in Eqs.(13)–(15) [17].

$$\nabla \cdot \left(\overline{\rho}\vec{\tilde{v}}\right) = 0 \tag{13}$$

$$\nabla \cdot \left(\overline{\rho}\vec{\tilde{v}}\vec{\tilde{v}}\right) = -\nabla\,\overline{p} + \nabla \cdot (\hat{\tau}) \tag{14}$$

$$\nabla \cdot \left(\overline{\rho}\vec{\tilde{v}}\left(\tilde{h} + \frac{\tilde{v}^2}{2}\right)\right) = \nabla \cdot \left(k_{eff}\nabla\tilde{T} - \sum_j \tilde{h}_j\vec{J}_j + \hat{\tau}\cdot\vec{\tilde{v}}\right) + \Omega \tag{15}$$

In Eqs.(13)–(15) p represents the pressure, $\hat{\tau}$ the total stress tensor, h the sensible enthalpy, k_{eff} the effective conductivity, J_j the diffusion flux of species j, and Ω the volumetric heat of chemical reactions. The total stress tensor $\hat{\tau}$ is formed by the sum of the laminar and turbulent stresses:

$$\hat{\tau}_{ij} = 2\left(\mu + \mu_t\right)\left(\tilde{S}_{ij} - \frac{1}{3}\frac{\partial\tilde{v}_k}{\partial x_k}\delta_{ij}\right) - \frac{2}{3}\bar{\rho}\kappa\delta_{ij} \tag{16}$$

with μ and μ_t indicating the laminar and turbulent dynamic viscosity, respectively, k the turbulent kinetic energy and S_{ij} the strain rate tensor, i.e.:

$$\tilde{S}_{ij} = \frac{1}{2}\left(\frac{\partial\tilde{v}_i}{\partial x_j} + \frac{\partial\tilde{v}_j}{\partial x_i}\right) \tag{17}$$

The turbulent viscosity is evaluated using the κ - ω Shear Stress Transport (SST) two-equations turbulence model developed by Menter [18]. The effective thermal conductivity k_{eff} is defined as:

$$k_{eff} = k + \frac{c_p\mu_t}{Pr_t} \tag{18}$$

where k is the laminar thermal conductivity, c_p is the specific heat capacity at constant pressure and Pr_t is the turbulent Prandtl number. In this work, Pr_t was selected to be 0.85 and the c_p is obtained as the mixture-average of the c_p of all the species in the mixture, while it is approximated by NASA7 polynomials [19] for the single species j, i.e.:

$$\frac{c_{p,j}(T)}{R} = a_{0,j} + a_{1,j}T + a_{2,j}T^2 + a_{3,j}T^3 + a_{4,j}T^4 \tag{19}$$

with R being the universal gas constant. Thus, the sensible enthalpy for the single species j in the case of ideal gas approximation is calculated as:

$$\tilde{h}_j = \int_{T_{ref}}^{T} c_{p,j}\,d\tilde{T} \tag{20}$$

with T_{ref} being 298.15 K. Then, the sensible enthalpy of the mixture is evaluated as:

$$\tilde{h} = \sum_j \tilde{Y}_j\tilde{h}_j \tag{21}$$

The diffusion flux of species j is defined as:

$$\vec{J}_j = -\left(D_{j,m} + \frac{\mu_t}{Sc_t}\right)\nabla\tilde{Y} - D_{\tilde{T},j}\nabla\tilde{T} \tag{22}$$

where Sc_t is the Schmidt number, Y is the mass fraction, $D_{j,m}$ is the molecular mass diffusion coefficient and $D_{T,j}$ is the Soret diffusion coefficient. In this study, the Schmidt number was set to 0.7.
Finally, the volumetric heat of reaction Ω is calculated as:

$$\Omega = -\sum_j \frac{h_j^0}{\mathcal{M}_j}\mathcal{R}_j \tag{23}$$

where h_j^0, $\mathcal{M}_j$ and $\mathcal{R}_j$ are the enthalpy of formation, the molecular weight and the volumetric rate of creation, respectively, of the j^{th} species.
In addition to Eqs. (13)–(15), a conservation equation is considered for $M-1$ species, where M denotes the total number of species in the mixture. The mass fraction of the excluded species is calculated as 1 minus the sum of the mass fractions of all the other species. To minimize the numerical error, N_2 is chosen to be the species not directly transported in the flow domain, as it is expected to have the largest mass fraction. These conservation equations are then written as:

$$\nabla \cdot \left(\bar{\rho}\vec{\tilde{v}}\tilde{Y}_j\right) = -\nabla \cdot \vec{J}_j + R_j \tag{24}$$

The reaction rates $\mathcal{R}_j$ are modelled using the Eddy-Dissipation Concept (EDC)[20], taking into account turbulence and chemistry interactions. The EDC model assumes that the reactions only occur in the *fine scales*, i.e. in the smallest turbulence scales. It is then necessary to calculate the volume of the computational cell that is occupied by these fine scales, i.e. the volume fraction κ_{fs}:

$$\kappa_{fs} = \frac{\xi^2}{1-\xi^2} \tag{25}$$

In Eq.25 the variable ξ represents the *length scale*, which is calculated as:

$$\xi = C_\xi \left(\frac{\nu\epsilon}{k^2}\right)^{\frac{1}{4}} \tag{26}$$

where C_ξ is a constant value equal to 2.1377, ν is the kinematic viscosity, k is the turbulent kinetic energy and ϵ is the rate of dissipation of turbulent kinetic energy. Moreover, the reactions are integrated over the *time scale* τ^*, which is defined as:

$$\tau^* = C_\tau \left(\frac{\nu}{\epsilon}\right)^{\frac{1}{2}} \tag{27}$$

where C_τ is a constant value equal to 0.4082. Finally, the reaction rates $\mathcal{R}_j$ can be written as [17]:

$$\mathcal{R}_j = \rho\kappa_{fs}\frac{Y_j^* - \tilde{Y}_j}{\tau^*} \tag{28}$$

where Y_j^* represents the fine-scale species mass fraction after reacting over the time scale τ^* in an adiabatic and isobaric perfectly stirred reactor, whose initial conditions are the species and temperature at the end of the previous iteration. Furthermore, the Fluent implementation of the EDC differs from the one originally proposed by Magnussen et al. in Ref.[21] as it does not take into account that reactions could occur only on a fraction of the fine scales, among other changes [22].
The spatial discretization is performed using second-order upwind schemes and the coupled pressure-velocity scheme. Finally, hydrogen chemistry is evaluated using the Ó Conaire reaction mechanism which encompasses 10 species (H, H_2, O, O_2, OH, H_2O, N_2, HO_2, H_2O_2, Ar) and 19 reaction steps [23].

B. Geometry Approximation and mesh

The 2D geometry fluid domain is built with the constraint that the inlets in the axisymmetric geometry have the same total area of the real combustor, to ensure that the fluid comes out of the inlets with the same velocity as it would in the real 3D geometry. The 2D geometry CAD with dimensions and boundary conditions used in this work is shown in Fig.2.

The 2D geometry of the radial swirler is approximated based on the actual swirler design, which features eight slots. Each slot has a total length of 25 mm, connected by two semicircular arcs with a radius of 2.25 mm. For a configuration with a geometric swirl number of 0.9, the slots are partially blocked by rings, obstructing 7 mm of their length.

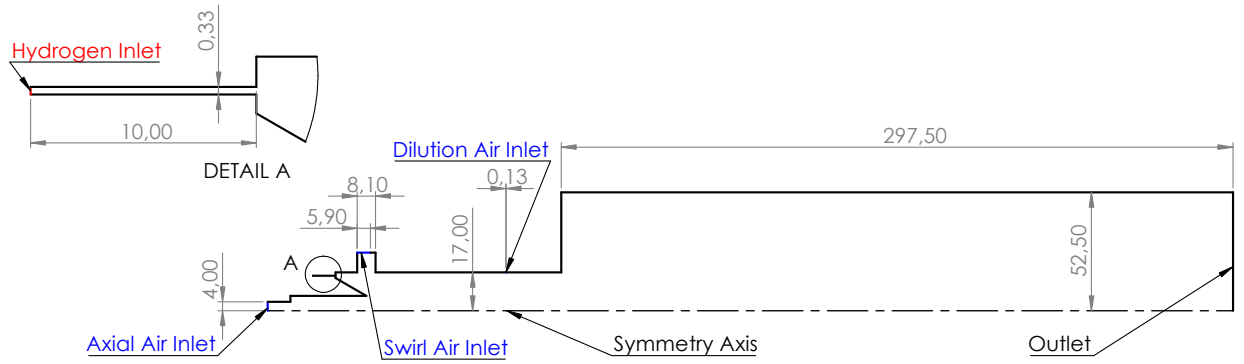

Fig. 2 Dimensions and boundary conditions of the 2D geometry simplification of the AHEAD combustor.

In the 2D axisymmetric approximation, the swirler is modeled with an inlet followed by a wall condition to represent the obstruction caused by the blocking rings. Since the continuous cylindrical surface in the 2D model represents the distributed area of the swirler slots, the inlet length in the simulation is shorter than the actual slot length. It is, therefore, necessary to determine the inlet position in the 2D approximation, and it was decided to retain the geometric centroid of the actual slot.

The same decision to retain the geometric centroid was applied in approximating the inlet area for both the fuel and the dilution air. In this approximation, the effect of the boundary layer occupying different portions of the injection orifice between the real and approximated geometry was neglected. Accounting for this would have required modifying the geometry of the fuel injection conduit as a function of the equivalence ratio. Additionally, to better approximate the inlet conditions of the hydrogen stream in the premixing tube, a portion of the fuel conduit is also included in the 2D geometry, which can be seen in Detail A in Fig.2. The resulting mesh is built with approximately $2 \cdot 10^5$ cells, dynamically refining cells to achieve a y^+ lower than 10 in every simulation. A mesh detail at the inlet can be observed in Fig.3.

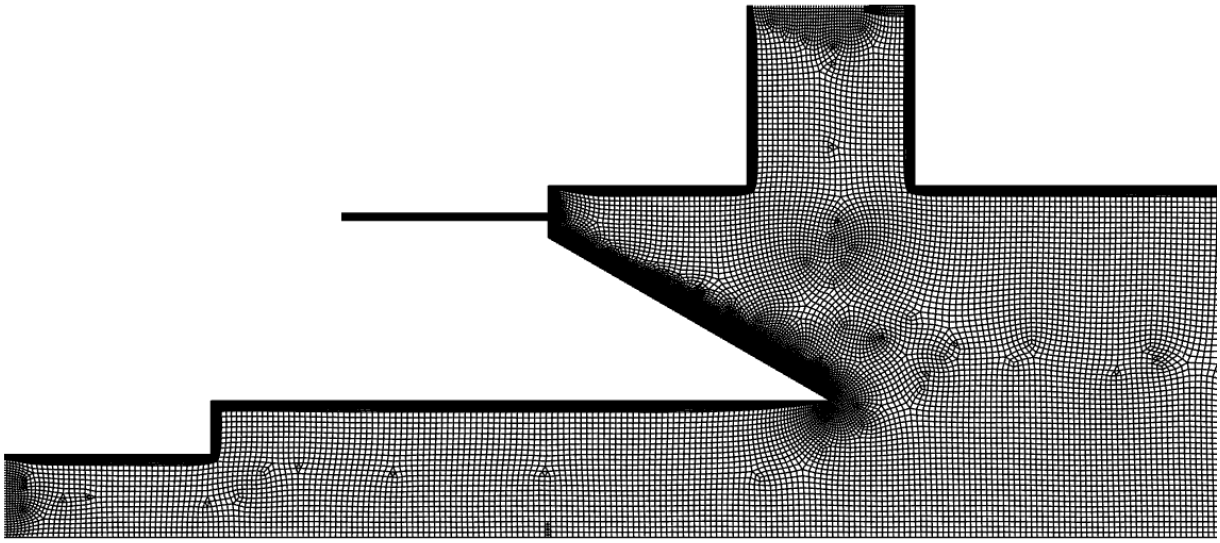

Fig. 3 Mesh detail.

Assuming that 2.5% of the total inlet air mass flow rate passes through the dilution orifices, the mass flow rates at

the boundaries are determined using the definition of the axial injection ratio, χ, as follows:

$$\begin{cases} \dot{m}_{\text{dil}} = 0.025\,\dot{m}_{\text{tot}} \\ \dot{m}_{\text{swirl}} = (1-\chi)\,(\dot{m}_{\text{tot}} - \dot{m}_{\text{dil}}) \\ \dot{m}_{\text{axial}} = \dot{m}_{\text{tot}} - \dot{m}_{\text{swirl}} - \dot{m}_{\text{dil}} \end{cases} \tag{29}$$

In Eq. 29, $\dot{m}_{\text{tot}}$ represents the total air mass flow rate, $\dot{m}_{\text{dil}}$ is the mass flow rate through the dilution orifices, $\dot{m}_{\text{axial}}$ is the mass flow rate through the axial orifice, and $\dot{m}_{\text{swirl}}$ is the mass flow rate through the swirl orifice.

Additionally, it is necessary to define the tangential velocity component at the swirler inlet. However, due to changes in the inlet geometry in the 2D RANS model, the geometrical swirl number can not be directly applied to establish boundary conditions. Instead, a tangential-to-radial velocity ratio of 0.8 at the swirler inlet was found to provide good agreement with experimental results, based on comparisons between CFD predictions and experimental PIV data for a single operating condition.

This approach aligns with the multi-fidelity model's objective to accommodate scenarios with limited HF data. However, it inherently reduces the accuracy of LF results since the selected tangential-to-radial velocity ratio may not be optimal for all the other operating conditions.

C. Low-Fidelity Results

The capability of the 2D axisymmetric simulations to capture key fluid dynamic characteristics is demonstrated through a comparison with experimental PIV data * for the following operating conditions: $\dot{m}_{\text{air}} = 180\,\text{kg/h}$, $T_{\text{air}} = 453\,\text{K}$, and $\phi = 0.4$.

Figure 4 compares the axial velocity v_z, normalized by the mixing tube velocity $u_0 = 70\,\text{m/s}$, between the experimental PIV measurements and the CFD simulation. The plot shows how axial velocity varies with radius r, normalized by the mixing nozzle radius $R = 34\,\text{mm}$, measured from the symmetry axis of the combustor. The comparison includes axial velocity profiles at different axial positions z/D, where $z = 0$ represents the end of the mixing tube. At $z/D = 0.043$, the RANS model accurately captures the axial velocity behavior observed experimentally at the mixing tube exit. As the axial position increases, the CFD results continue to closely follow the experimental data, with the axial velocities becoming nearly identical between RANS and PIV at one of the farthest measured points, i.e. $z/D = 2.687$.

Analogous considerations can be applied for the comparison of the radial velocity v_r between PIV and RANS, performed in the same axial locations and shown in Fig.5. Similarly, it is possible to appreciate how the RANS resembles the global trend shown by the PIV. This shows the capability of the RANS simulation to capture the inner and outer recirculation zones inside the combustion chamber.

Additionally, Fig. 6 illustrates the flame behavior as a function of the equivalence ratio for an inlet temperature of 453 K and an air inlet mass flow rate of 180 kg/h, with heat of reaction contours normalized by their maximum values in each simulation to facilitate comparison. In Fig. 6, the white bar extending up to $r/D = 0.5$ represents the length of the mixing tube, while the blue bar indicates the combustion chamber wall. The trends observed in the simulations align well with experimental results from Ref. [8], based on post-processed OHPLIF data. Specifically, in the experiments, the flame lifts off until the equivalence ratio reaches 0.5, at which point it attaches to the end of the mixing tube. This behavior is captured by the RANS model, with the key difference being that the flame attachment is predicted to occur at $\phi = 0.6$.

Another discrepancy between the simulation and experimental results arises at the stoichiometric equivalence ratio. In the experimental data, a pronounced curvature of the flame is observed, while the RANS model predicts a relatively flatter flame surface. This difference in behavior may stem from the limitations of the turbulence model, which might not fully capture the complexities of the swirled flow. Nevertheless, despite these discrepancies, the RANS model successfully reproduces the overall trend observed in the experimental data, suggesting that the low-fidelity model holds significant potential for accurately representing the complex fluid dynamics within the combustor chamber.

Finally, it is worth noticing that the average computational time for the generation of a single LF data point is on the order of $O(7\,\text{CPU}\cdot\text{h})$, using 30 *Intel® Xeon® Gold 6338* cores.

*PIV data can be downloaded from the following URL: https://tnfworkshop.org/ahead-lean-premixed-swirl-stabilized-hydrogen-burnertu-berlin/. URL visited on May 20th, 2024.

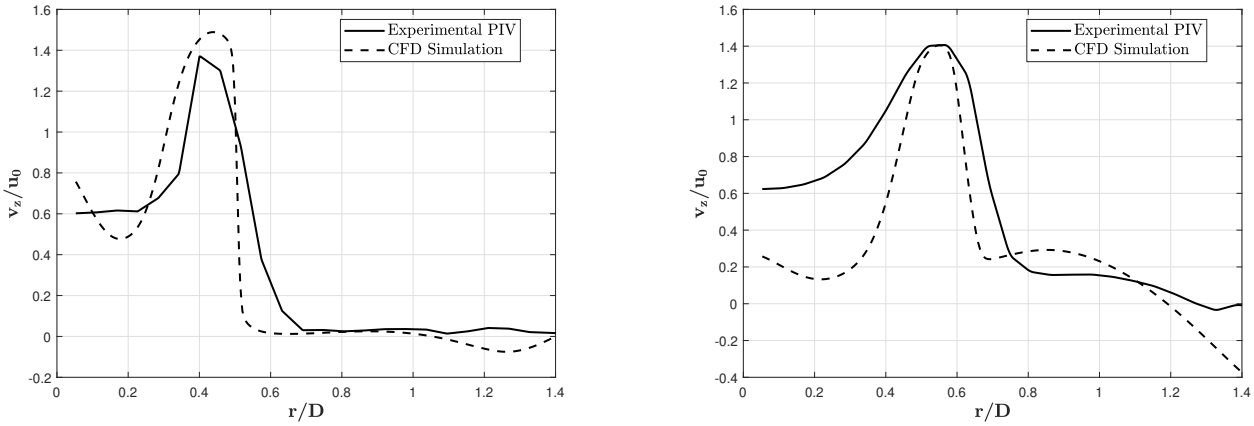

(a) z/D = 0.043

(b) z/D = 0.335

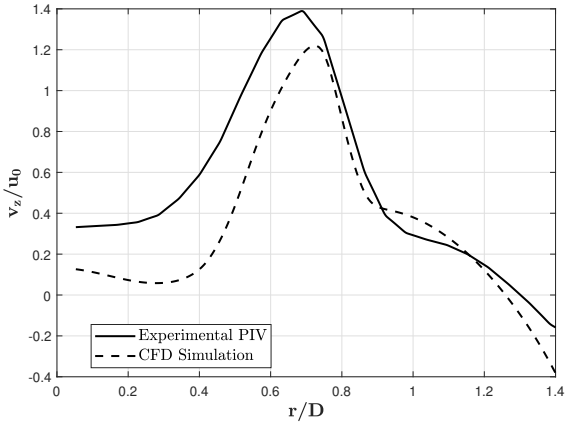

(c) z/D = 0.629

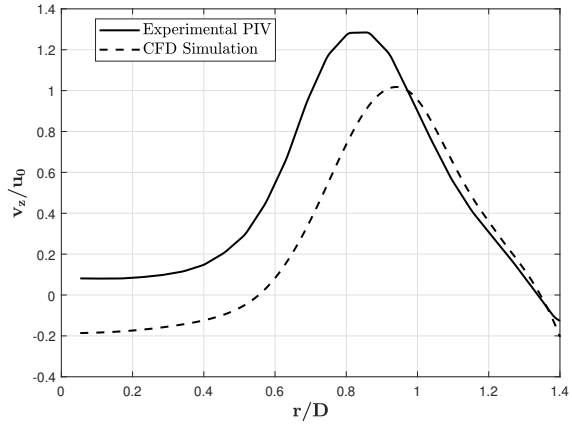

(d) z/D = 0.923

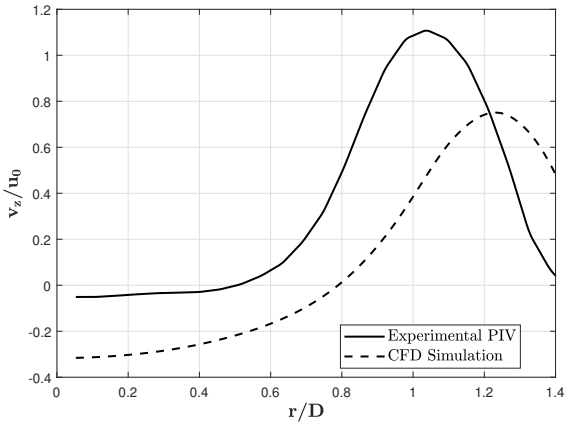

(e) z/D = 1.217

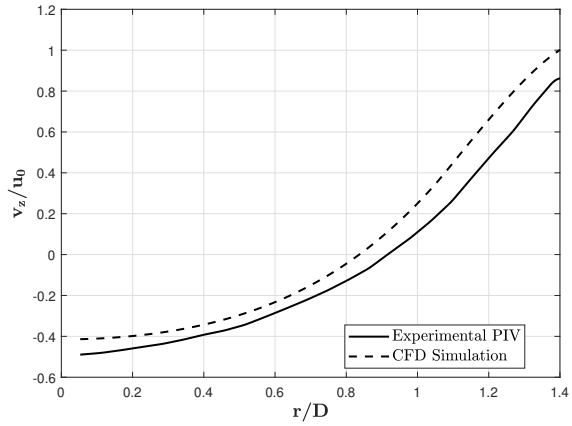

(f) z/D = 2.687

Fig. 4 Comparison of axial velocity v_z, normalized by velocity u_0, between PIV and CFD data at different axial locations z and radius r, normalized by mixing tube diameter D.

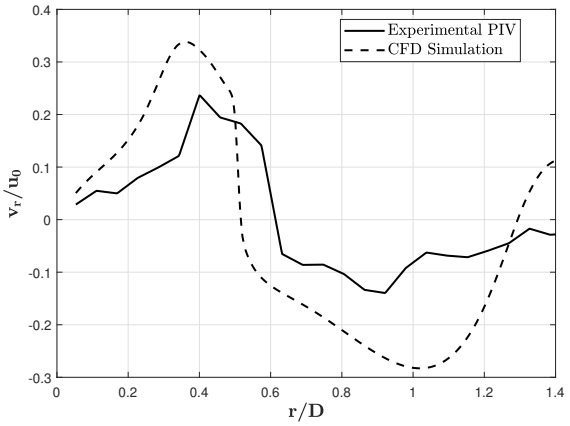

(a) z/D = 0.043

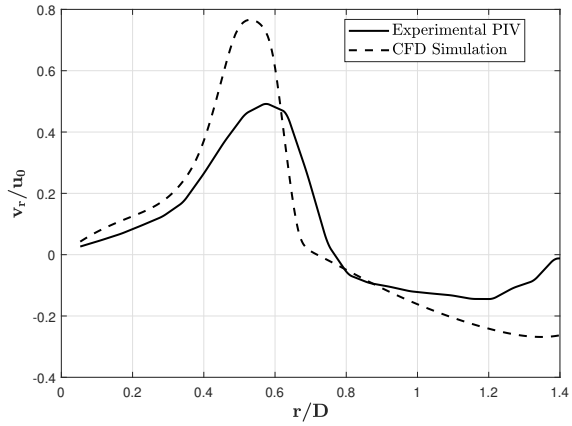

(b) z/D = 0.335

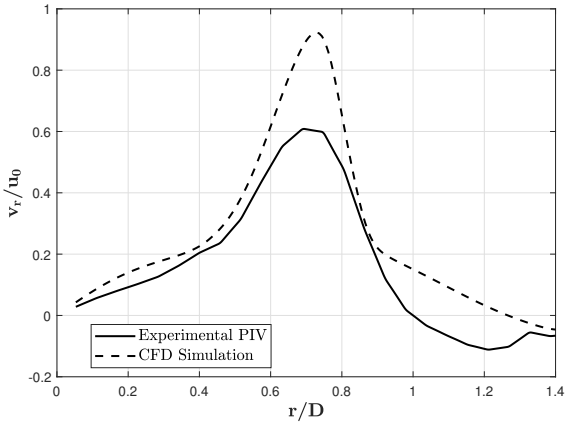

(c) z/D = 0.629

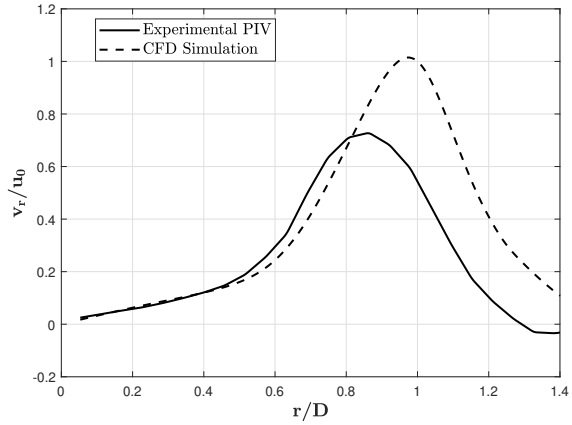

(d) z/D = 0.923

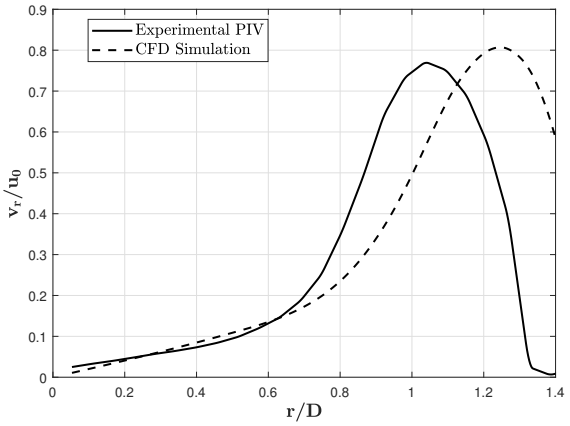

(e) z/D = 1.217

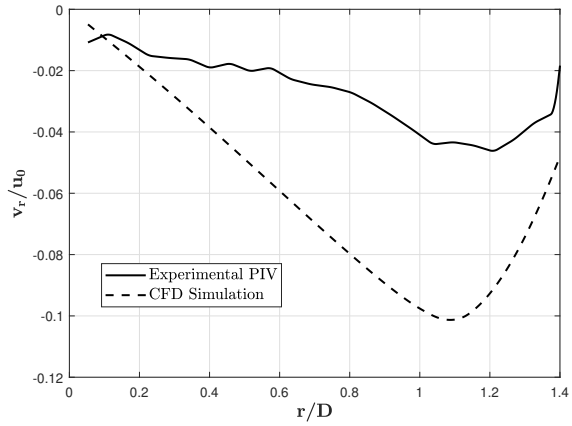

(f) z/D = 2.687

Fig. 5 Comparison of radial velocity v_r, normalized by velocity u_0, between PIV and CFD data at different axial locations z and radius r, normalized by mixing tube diameter D.

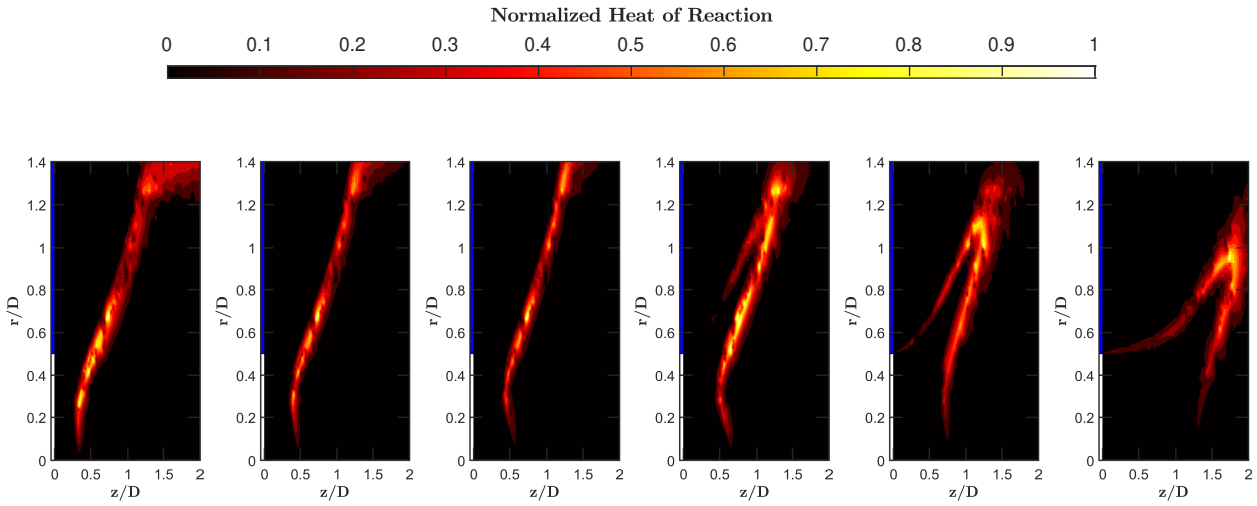

(a) $\phi = 0.3$ **(b)** $\phi = 0.4$ **(c)** $\phi = 0.5$ **(d)** $\phi = 0.6$ **(e)** $\phi = 0.8$ **(f)** $\phi = 1.0$

Fig. 6 CFD flame visualization through the heat of reaction contours. Simulations performed at $T_{in} = 453\,K$, and $m_{air} = 180\,kg/h$.

Finally, Fig. 7 presents a comparison between the RANS output (low-fidelity data) and the experimental results (high-fidelity data). The flame distance for the low-fidelity data is determined from the CFD results, using the first axial position where the heat of reaction exceeds a threshold of 1 W. The Pearson's linear correlation coefficient between the low-fidelity and high-fidelity data is found to be 0.77, which supports the assumption of a linear correlation between these datasets, as discussed in Section III.

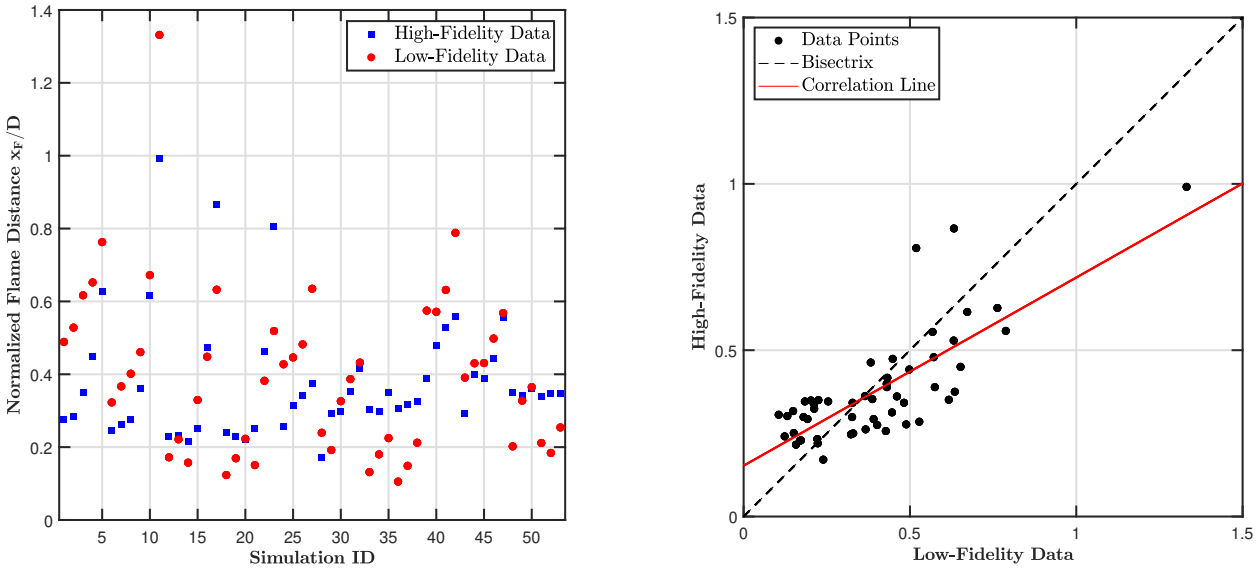

(a) **(b)**

Fig. 7 (a) High-Fidelity and Low-Fidelity data comparison and (b) linear correlation between the two different fidelity levels.

VI. Multi-Fidelity Results

To validate the multi-fidelity model, 15 points are randomly selected from Table 1 as validation points and they are explicitly shown in Eq.30. These points are chosen such that they do not lie at the boundaries of the parameter space, meaning none of the selected points have air temperature, air mass flow rate, or equivalence ratio values that correspond to the minimum or maximum values within the dataset. The parameter space is thus defined by air mass flow rate, air temperature, and equivalence ratio.

$$ID_{validation} = [7,\ 8,\ 10,\ 13,\ 14,\ 15,\ 16,\ 29,\ 32,\ 33,\ 44,\ 45,\ 46,\ 47,\ 48] \tag{30}$$

For the remaining points in the dataset, a sequence of training points is constructed by iteratively adding the point that is furthest from the existing points in the sequence. To obtain the statistics over the error in Fig.8 the training set construction was performed each time starting from a different point between the 38 ones in the dataset.

The multi-fidelity model is compared to a single-fidelity model which fits the HF data with RBF using the same HF training points of the multi-fidelity model, which in this work uses RBF too to approximate the correction field $\delta(x)$.

The results, shown in the boxplot in Fig. 8, with the solid central line representing the median, demonstrate that the multi-fidelity model consistently outperforms both the high-fidelity fitting and the individual low-fidelity data in terms of root mean square error. Notably, the multi-fidelity model remains effective even with a small set of training points, approximately equal to the number of input parameters. As the number of training points increases, the model becomes less sensitive to the specific points selected, progressively improving the low-fidelity data until it reaches an asymptote with just five training points.

Moreover, increasing the number of training points also reduces the error for the high-fidelity fitting, which, however, plateaus at a higher asymptote compared to the multi-fidelity model. This highlights the multi-fidelity model's ability to effectively enhance low-fidelity data.

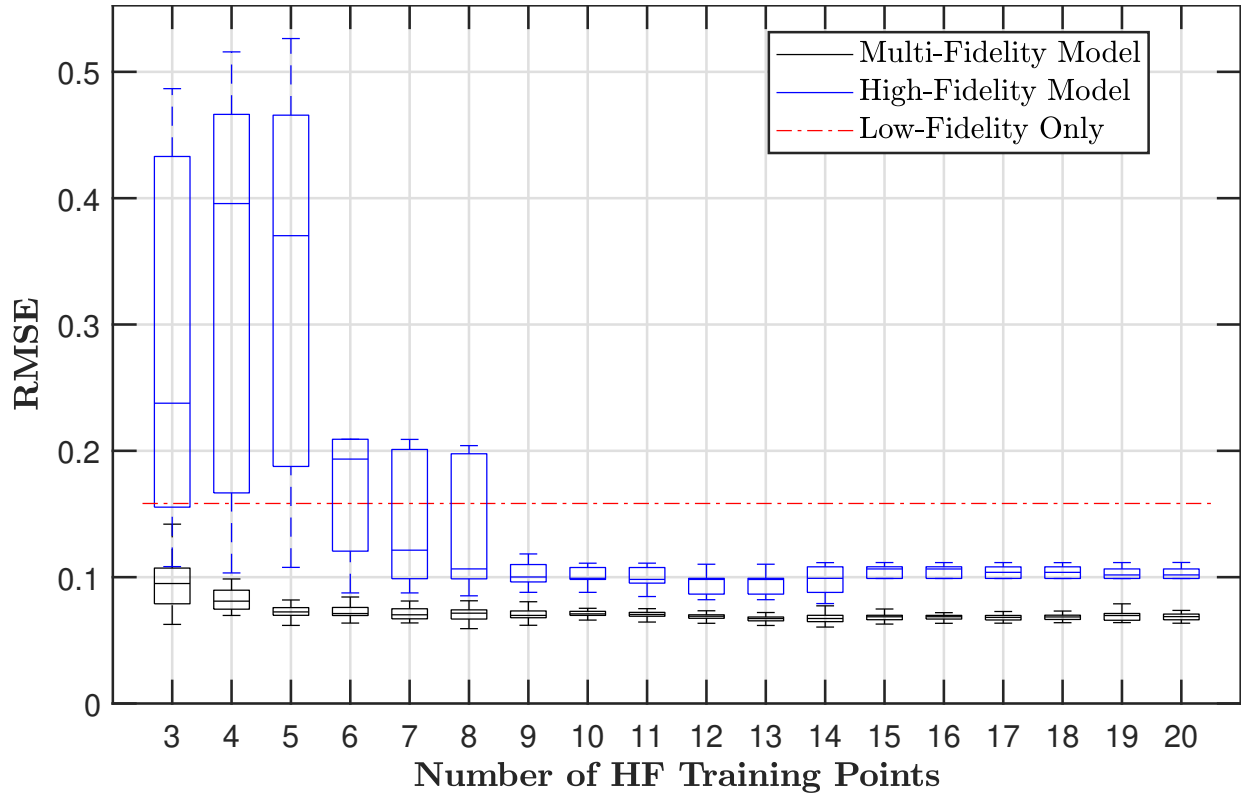

Fig. 8 Comparison of high-fidelity and multi-fidelity models RMSE computed on a fixed validation set. Statistics are obtained by changing the training set sequences. Outliers are omitted.

Finally, the online computational cost of the multi-fidelity model, including both the training and evaluation phases, is on the order of $O(1 \cdot 10^{-4}\,\text{CPU} \cdot \text{h})$. Thus, the increase in computational cost due to the multi-fidelity model is

negligible concerning the generation of low-fidelity data.

VII. Conclusions

A multi-fidelity modeling approach is presented, assuming a linear correlation between LF and HF data. The model is trained and validated to predict the flame distance from the mixing nozzle in a lean premixed swirl-stabilized hydrogen burner. The experimental data from Ref. [8] serve as the HF dataset, while the LF data are obtained using 2D axisymmetric RANS simulations. The output of CFD simulations reveals a linear correlation between HF and LF data, demonstrating that RANS simulations, despite the simplification of a 2D axisymmetric geometry and the limitation on approximating inlet boundary conditions, can effectively capture the complex fluid dynamics and chemistry-turbulence interactions within the combustion chamber.

Additionally, the multi-fidelity model enhances the LF predictions by leveraging a limited number of HF data points, using RBF to construct a correction field between HF data and LF approximations. This approach successfully approximates a complex phenomenon, such as flame positioning in a hydrogen burner, by integrating LF simulations with sparse HF data. The methodology offers significant potential for reducing experimental costs, facilitating the exploration of design parameters, and improving the design of experiments. Furthermore, HF data could be substituted with higher-fidelity simulations, such as large-eddy simulations (LES), or extended through intermediate-fidelity layers, like 3D RANS with more accurate turbulence modeling, bridging the gap between computational and experimental results.

Acknowledgments

The present research is funded by the Italian Ministry of University and Research under the National Recovery and Resilience Plan - PNRR (Ministerial Decree 351/2022).

AI software has been used for text review and grammar check to improve readability and fluency of English text written by non-native authors.

References

[1] Adler, E. J., and Martins, J. R., "Hydrogen-powered aircraft: Fundamental concepts, key technologies, and environmental impacts," *Progress in Aerospace Sciences*, Vol. 141, 2023, p. 100922. https://doi.org/https://doi.org/10.1016/j.paerosci.2023.100922, special Issue on Green Aviation.

[2] Skottene, M., and Rian, K. E., "A study of NOx formation in hydrogen flames," *International Journal of Hydrogen Energy*, Vol. 32, No. 15, 2007, pp. 3572–3585. https://doi.org/https://doi.org/10.1016/j.ijhydene.2007.02.038, international Symposium on Solar-Hydrogen-Fuel Cells 2005.

[3] Brand, J., Sampath, S., Shum, F., Bayt, R., and Cohen, J., "Potential Use of Hydrogen In Air Propulsion," *AIAA International Air and Space Symposium and Exposition: The Next 100 Years*, 2003. https://doi.org/10.2514/6.2003-2879.

[4] Schefer, R. W., White, C., and Keller, J., "Chapter 8 - Lean Hydrogen Combustion," *Lean Combustion*, edited by D. Dunn-Rankin, Academic Press, Burlington, 2008, pp. 213–VIII. https://doi.org/https://doi.org/10.1016/B978-012370619-5.50009-1.

[5] Benim, A. C., and Syed, K. J., *Flashback mechanisms in lean premixed gas turbine combustion*, Academic Press, Waltham, Massachusetts, 2015. https://doi.org/10.1016/C2013-0-18847-2.

[6] Zhou, H., Xue, J., Gao, H., and Ma, N., "Hydrogen-fueled gas turbines in future energy system," *International Journal of Hydrogen Energy*, Vol. 64, 2024, pp. 569–582. https://doi.org/https://doi.org/10.1016/j.ijhydene.2024.03.327.

[7] Reichel, T. G., and Paschereit, C. O., "Interaction mechanisms of fuel momentum with flashback limits in lean-premixed combustion of hydrogen," *International Journal of Hydrogen Energy*, Vol. 42, No. 7, 2017, pp. 4518–4529. https://doi.org/https://doi.org/10.1016/j.ijhydene.2016.11.018.

[8] Reichel, T. G., Goeckeler, K., and Paschereit, O., "Investigation of Lean Premixed Swirl-Stabilized Hydrogen Burner With Axial Air Injection Using OH-PLIF Imaging," *Journal of Engineering for Gas Turbines and Power*, Vol. 137, No. 11, 2015, p. 111513. https://doi.org/10.1115/1.4031181.

[9] Fernández-Godino, M. G., "Review of multi-fidelity models," *Advances in Computational Science and Engineering*, Vol. 1, No. 4, 2023, pp. 351–400. https://doi.org/10.3934/acse.2023015.

[10] Kennedy, M., and O'Hagan, A., "Predicting the output from a complex computer code when fast approximations are available," *Biometrika*, Vol. 87, No. 1, 2000, p. 1–13. https://doi.org/https://doi.org/10.1093/biomet/87.1.1.

[11] Meng, X., and Karniadakis, G. E., "A composite neural network that learns from multi-fidelity data: Application to function approximation and inverse PDE problems," *Journal of Computational Physics*, Vol. 401, 2020, p. 109020. https://doi.org/https://doi.org/10.1016/j.jcp.2019.109020.

[12] Buhmann, M., *Radial Basis Functions: Theory and Implementations*, Cambridge University Press, 2003. https://doi.org/10.1017/CBO9780511543241.

[13] Rasmussen, C. E., and Williams, C. K. I., *Gaussian processes for machine learning*, Adaptive computation and machine learning, MIT Press, 2006. https://doi.org/https://doi.org/10.7551/mitpress/3206.001.0001.

[14] Optimad, "romBOX," , 2024. URL https://www.optimad.it/.

[15] Tanneberger, T., Reichel, T. G., Krüger, O., Terhaar, S., and Paschereit, C. O., "Numerical Investigation of the Flow Field and Mixing in a Swirl-Stabilized Burner With a Non-Swirling Axial Jet," *Turbo Expo: Power for Land, Sea, and Air, Volume 4B: Combustion, Fuels and Emissions*, 2015, p. V04BT04A026. https://doi.org/10.1115/GT2015-43382.

[16] Reichel, T. G., Terhaar, S., and Paschereit, O., "Increasing Flashback Resistance in Lean Premixed Swirl-Stabilized Hydrogen Combustion by Axial Air Injection," *Journal of Engineering for Gas Turbines and Power*, Vol. 137, No. 7, 2015, p. 071503. https://doi.org/10.1115/1.4029119.

[17] *Ansys ® Fluent, Release 2024 R1 - Theory Guide*, ANSYS, Inc., 2024.

[18] Menter, F. R., "Two-equation eddy-viscosity turbulence models for engineering applications," *AIAA Journal*, Vol. 32, No. 8, 1994, pp. 1598–1605. https://doi.org/10.2514/3.12149.

[19] McBride, B. J., Gordon, S., and Reno, M. A., *Coefficients for calculating thermodynamic and transport properties of individual species*, Vol. 4513, NASA Langley Research Center, 1993. URL https://ntrs.nasa.gov/citations/19940013151.

[20] Magnussen, B. F., "The eddy dissipation concept: A bridge between science and technology," *ECCOMAS thematic conference on computational combustion*, Vol. 21, Lisbon, Portugal, 2005, p. 24. URL https://folk.ntnu.no/ivarse/edc/BFM_ECOMAS2005_Lisboa.pdf.

[21] Gran, I. R., and Magnussen, B. F., "A Numerical Study of a Bluff-Body Stabilized Diffusion Flame. Part 2. Influence of Combustion Modeling And Finite-Rate Chemistry," *Combustion Science and Technology*, Vol. 119, No. 1-6, 1996, pp. 191–217. https://doi.org/10.1080/00102209608951999.

[22] Ertesvåg, I. S., "Scrutinizing proposed extensions to the Eddy Dissipation Concept (EDC) at low turbulence Reynolds numbers and low Damköhler numbers," *Fuel*, Vol. 309, 2022, p. 122032. https://doi.org/https://doi.org/10.1016/j.fuel.2021.122032.

[23] Ó Conaire, M., Curran, H. J., Simmie, J. M., Pitz, W. J., and Westbrook, C. K., "A comprehensive modeling study of hydrogen oxidation," *International Journal of Chemical Kinetics*, Vol. 36, No. 11, 2004, pp. 603–622. https://doi.org/https://doi.org/10.1002/kin.20036.